Cement and Concrete Research 143 (2021) 106390

Contents lists available at ScienceDirect

Cement and Concrete Research

journal homepage: www.elsevier.com/locate/cemconres

Monitoring steel fibre orientation in self-compacting cementitious composite slabs during pouring with dynamic X-ray radiography

Benjy Marks [a], Marta Miletić [b], Bernard Cheuk Hay Lee [a], Muhammad Hazim Zia [a], Joaquim A. O. Barros [c], Daniel Dias-da-Costa [a,*]

[a] School of Civil Engineering, The University of Sydney, Sydney, NSW 2006, Australia
[b] Department of Civil, Construction, and Environmental Engineering, San Diego State University, San Diego, CA 92182-1324, USA
[c] ISISE, Dep. Civil Eng., School Eng., University of Minho, Campus de Azurém, 4800-058 Guimarães, Portugal

ARTICLE INFO

Keywords:
Fibre orientation
Self-compacting cementitious composite
Steel fibre reinforced cementitious composite
Dynamic X-ray radiography

ABSTRACT

This paper presents a new technique based on dynamic X-ray radiography that can be used to assess fibre orientation during pouring of steel fibre reinforced cementitious composites. Synthetic examples were used to assess the suitability and robustness of the technique, which was shown to provide reliable measurements of fibre orientation even when the signal-to-noise ratio is relatively high. A study was then carried out on the effect of formwork aspect ratio, time/duration of pouring, and rebar placement on the fibre orientation while pouring self-compacting cementitious composite slabs. Results demonstrated the ability of the technique in monitoring the movements of fibres while pouring, and the strong effect of the flow in inducing preferential fibre alignment within the slabs. Fibre orientation was found to vary progressively over time and could take about half of the duration of pouring to fully stabilise.

1. Introduction

Steel fibre reinforced self-compacting cementitious composites are a bi-functional cement-based material that benefits from high flowability and post-cracking tensile capacity provided by fibre reinforcement mechanisms [1,2]. The addition of fibres also ensures a more diffused cracking process with smaller widths, which contributes to enhanced durability. The combination of self-compacting cementitious composite (SCC) and fibre reinforced cementitious composite (FRC) technologies has a high potential for accomplishing significant gains in engineering performance and economy owing to the elimination of vibration and reduction or even complete substitution of conventional reinforcement [3].

The performance of FRC is highly dependent on the concrete strength, as well as on the fibre content, geometry and type [4,5]. In addition, the residual strength of FRC is strongly dependent on the distribution and orientation of fibres within the cement matrix at the end of pouring [6–10]. Fibres aligned in the direction of tensile stresses are preferential for a member loaded in one direction. The efficiency of fibres decreases from 100% when aligned along the direction of tensile stress to 30% when randomly distributed [11]. A random fibre orientation can be beneficial for members acting without a preferential stress field [12]. Therefore, it is important to properly understand and control the factors related to fibre orientation to ensure that the required — or even enhanced — material and structural performance is obtained for real applications [13,14]. This will also support the development of more accurate computational models for predicting and designing fibre reinforced composites, which are capable of taking into account the explicit location of the fibres [15].

A non-comprehensive understanding of the effects of fibre orientation on mechanical properties of fibre reinforced concrete is limiting the confidence of designers for the use of this composite in developing innovative construction systems [16]. A range of factors impacts fibre distribution and orientation, which include type and length of fibre [17–19], volumetric fibre content [20,21], specimen size and shape [16], concrete flowability, reinforcement layout [22], and casting process [6,23,24]. Concerning the latter, conditions for preferential orientation can be created by geometrical restrictions and shear stresses caused by concrete flow [22], placing methodologies, and compaction process [25]. Flow- and gravity-induced segregation of fibres into layers may also occur while concrete is placed and left to cure [26].

The effect of specimen geometry on fibre orientation and resulting

* Corresponding author.
E-mail address: daniel.diasdacosta@sydney.edu.au (D. Dias-da-Costa).

https://doi.org/10.1016/j.cemconres.2021.106390
Received 24 June 2020; Received in revised form 28 September 2020; Accepted 31 January 2021

Table 1
Specimen and fibre dimensions reported in the literature.

Authors	Specimen			Fibre		
	Height (mm)	Width (mm)	Length (mm)	Type	Diameter (mm)	Length (mm)
Abrishambaf et al. [29]	60	1000	1600	Hooked-end	0.55	33
Andries et al. [18]	150	150	600	Hooked-end	0.9	30/60
Ferrara et al. [3]	30	500	1000	Straight	0.16	13
Lameiras et al. [31]	150	150	600	Hooked-end	0.55	35
Sanal and Zihnioglu [16]	50	100/200/300	500	–	0.16	6/13
Stähli et al. [32]	90	900	1800	Straight	0.6	30
Suuronen et al. [33]	25	1000	5000	Hooked-end	1	50
Zerbino et al. [34]	90	1800	925	Hooked-end	0.45	35

mechanical performance was studied by Sanal and Zihnioglu [16] for 25 and 50 mm thick concrete slabs. The width of the structural element can indeed constrain fibres to align in the longitudinal direction of the member, particularly in the case of fibres with lengths of the same order as the width of the specimen. Such an increase in the direction of gravity can decrease the flexural strength of the member given that fibres crossing the flexural cracks are not efficiently oriented for resisting the principal tensile stresses which are nearly orthogonal to the planes of those cracks.

Barnett et al. [27] studied the flow of concrete in three round concrete panels and observed the tendency of fibres to align orthogonally to the radius when poured in the centre, and parallel to the radius when poured near the formwork edge. It was also found that the panel poured from the centre had the highest anisotropy, followed by the panel poured near the edge and by the panel poured randomly. It was noted that although the panel poured from the centre was the most anisotropic, image analysis showed the concrete in that region to be indeed isotropic. This is because the fibres are not affected by the radial flow there. It is worth mentioning that the panel poured from the centre had the highest flexural strength, followed by the panel poured randomly, and by the panel poured near the formwork, which was the weakest. The strongest panel was 1.7× stronger than the weakest, which shows that if adequate control measures are in place, concrete flow can be used to have a positive impact on fibre orientation and structural strength.

Theoretically, SCC flows radially outwards from the point of pouring. If concrete is left unconstrained, it would continue to flow radially [28,29], such as when formwork edges are at a significant distance away from the pouring [3] or when specimens are of circular shape [27]. However, SCC begins to flow parallel to formwork edges in specimens where the flow is constrained by those edges [30]. The presence of rebars also constraints concrete flow similarly to formwork edges [22]. Table 1 summarises some of the additional studies found in the scope of SCC FRC slabs, including their specimen dimensions and fibre properties.

Several methods exist for measuring fibre orientation inside cast concrete panels, with either image analysis using optical microscopy [10], scanning electron microscopy [35] or X-ray radiography [36–39]. Although the image analysis is a relatively simple method, the main drawback is that the FRC specimen needs to be cut in thin slices, and the sample faces need to be polished to make fibres and other material constituents visible before taking high-resolution 2D images. Thus, the destructive sectioning of specimens is not ideal for obtaining a complete 3D description of fibre orientation and distribution in the volume [40].

There are alternative non-destructive methods such as electrical resistivity [41] and electrochemical-impedance spectrometry tests [42,43]. These relate the electrical properties of FRC to the fibre orientation and distribution. However, their main shortcomings are that they only assess fibre orientation and distribution tendencies, and can only be applied to FRC with conductive fibres.

The previously aforementioned challenges can be resolved with 3D computed tomography (CT) scanning and advanced 3D image reconstruction techniques [33,44–52]. X-ray based CT scanning is a promising method that can be used to find each individual fibre. A summary of some of the important CT-based investigations on fibre orientation and distribution in FRC over the last decade is presented in [53]. Despite the advantages and availability of modern X-ray CT tools, powerful computational resources, and advanced image processing techniques, the analysis of FRC samples poses several specific challenges. For example, many fibres remain in contact with each other inside samples, which makes their individual analysis in images difficult. Also, the bleeding effect in FRC tomograms renders the fibres thicker and exacerbates the problem of contact between fibres in the tomograms. Furthermore, since X-ray CT scanning requires long scanning times, small specimens are preferred for imaging, which are typically cored from different locations of a structure to be able to effectively map the fibre dispersion across the whole structure. This renders X-ray CT unsuitable to study the real-time flowing properties of cementitious composite.

Having taken into account the limitations of existing techniques and the interest in monitoring the fibre distribution in the self-compacting cementitious composite while pouring, an innovative approach using dynamic X-ray radiography is proposed in this paper. The technique enables the ability to monitor the flow of fibres during pouring and to track the changes in orientation, despite the natural agglomerations and interactions of fibres. The technique is applied to provide experimental evidence and data to help understand how cementitious composite flow relates to fibre reorientation of small SCC FRC slabs. The slabs were continually monitored during pouring until fibres were in their ultimate position. Given the importance of boundary constraints introduced by formwork edges and specimen size [3,11], a range of specimens with varying aspect (width to length) ratio was considered and compared.

The paper is outlined as follows. In the next section, the X-ray radiography technique is presented together with the main principles governing the detection of fibre orientation. Synthetic examples are used to validate the applicability of the technique and assess its ability to measure orientation. In Section 3, the experimental programme, selection of specimen sizes, and materials used are presented. Results and their discussion are given in Section 4, whereas Section 5 summarises the main findings.

2. X-ray radiography

X-ray radiation can be used to image the interior of specimens. The specimen is typically located between a source of X-rays and a detector panel. The detector panel measures the intensity of the X-ray beam after passing through the specimen. The nature of X-ray radiation is such that the intensity of X-rays exponentially decay as they pass through matter, following:

$$F = F_0 e^{-\alpha l}, \tag{1}$$

where F is the intensity of X-rays measured at the detector panel, F_0 is the intensity at the source, α is the attenuation coefficient, which is material dependent, and l is the path length of the X-rays passing through the material. A material with a large attenuation coefficient, such as steel, absorbs a higher number of X-rays than a material with a lower attenuation coefficient, such as aggregates, cement and water. For this reason, it is relatively straightforward to distinguish macroscopic steel fibres within a cementitious composite matrix when illuminated with X-ray radiography. In this work, advanced image analysis

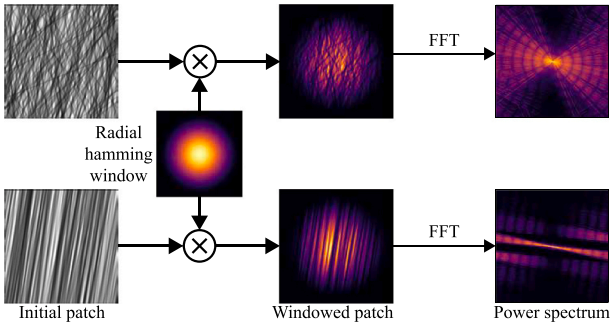

Fig. 1. Schematic representation of the orientation algorithm. *Top*: Poorly aligned fibres. *Bottom*: Well aligned fibres. In each case, an initial patch is taken from a larger image, which is then multiplied by a radial Hamming window and then processed with a 2D Fourier transform (FFT). Aligned fibres are evident as streaks in the FFT that are orthogonal to the original fibre orientation. Note that the power spectrum is presented on a log scale.

techniques are proposed to find the statistical properties of the radiographs themselves, without distinguishing between the solid matrix and the steel fibres.

2.1. Fibre orientation measurement

A technique by Guillard et al. [54], Jiang et al. [55], originally validated against manual measurements of the orientation of individual fibres mixed in with rice and lentils, is herein implemented to assess the orientation of steel fibres in SCC. A summary of the method in the context of fibre orientation is shown in Fig. 1. The proposed algorithm works by calculating a two-dimensional power spectrum of a given radiograph (or image), which describes the frequency distribution of the intensities recorded in the radiograph. In this instance, since the radiograph represents physical space, the frequencies can be inverted to give spatial wavelengths. This two-dimensional wavelength space is related to the spatial domain of the original image. If more power is found along a specific direction in the wavelength space, a preferential direction of the fibres can be inferred. The magnitude of the alignment can then also be related to the strength of the alignment in the power spectrum. Specifically, images are split into square patches of width w pixels and normalised to have zero mean and standard deviation of one. A two-dimensional Fourier transform of a patch can be expressed as:

$$S(\boldsymbol{k}) = \left| \iint F(\boldsymbol{x}) \times \mathscr{W}(\boldsymbol{r}(\boldsymbol{x})) e^{2i\pi \boldsymbol{k}\cdot\boldsymbol{x}}\, d\boldsymbol{x} \right|^2, \tag{2}$$

where S is the power spectrum, $\boldsymbol{k} = (k_x, k_y)$ the wavevector, $F(\boldsymbol{x})$ the normalised X-ray intensity at location $\boldsymbol{x}$ and $\mathscr{W}(\boldsymbol{r}) = cos(2\pi r/w)/2$ is the radial hamming window, with $\boldsymbol{r}$ being the vector from the centre of the patch to a given pixel.

As is done commonly when modelling liquid crystals [56], a structure tensor, $\boldsymbol{Q}$, is created, and by summing the structure tensor weighted by the power spectrum, a nematic order tensor $\boldsymbol{T}$, can be produced as:

$$\boldsymbol{Q}(\boldsymbol{k}) = \frac{1}{\Delta k_x \Delta k_y} \int_{k_x-\Delta k_x/2}^{k_x+\Delta k_x/2} \int_{k_y-\Delta k_y/2}^{k_y+\Delta k_y/2} \frac{\boldsymbol{k}\otimes\boldsymbol{k}}{|\boldsymbol{k}|^2}\, d\boldsymbol{k}, \tag{3}$$

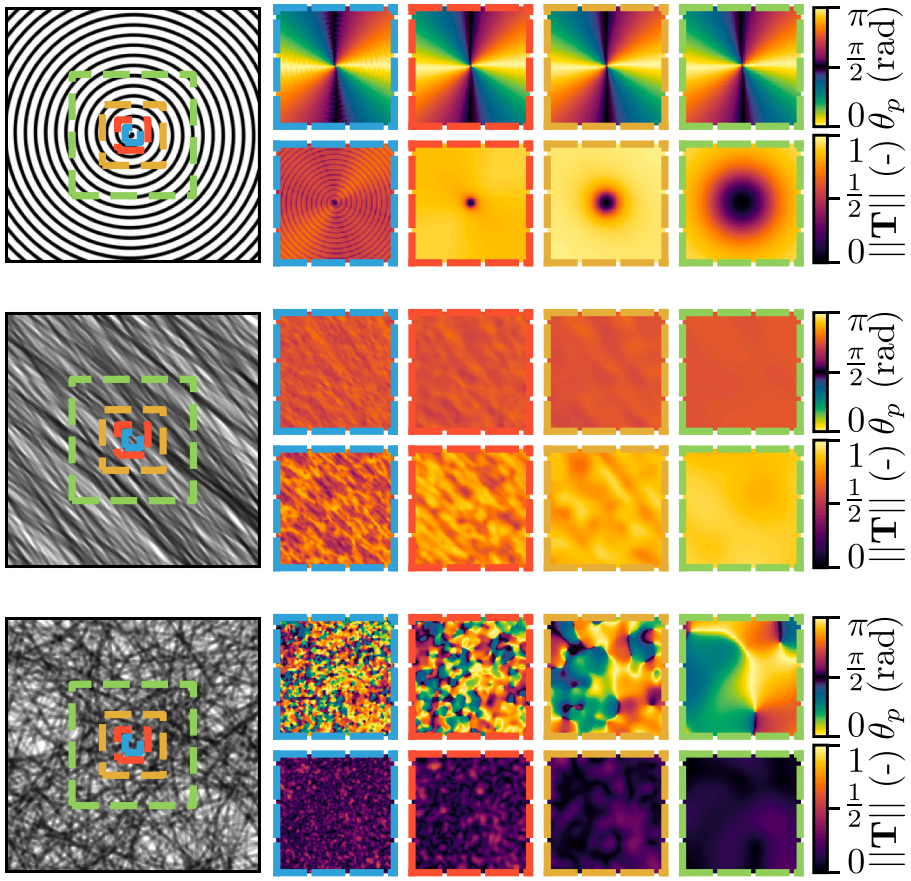

Fig. 2. Three examples of the performance of the orientation algorithm. *Left*: Original images. For each horizontal strip *Top rows*: Principal orientation field θ_p. *Bottom rows*: Alignment magnitude field $\|\boldsymbol{T}\|$. From left to right, increasing patch width. The colour of the border of each image indicates the patch size used to produce it, as shown with the correspondingly coloured dashed lines on the original images.

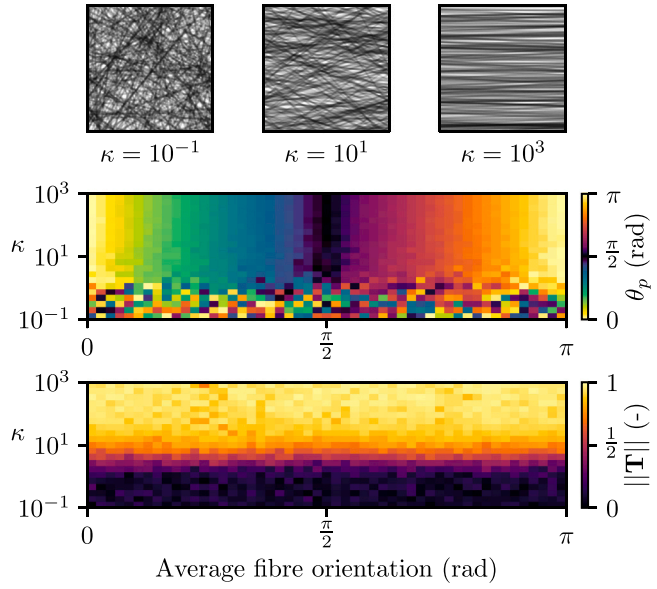

Fig. 3. Validation of the image analysis technique for idealised fibres. *Top*: Three examples of artificial radiographs of idealised fibre orientation profiles with principal angle of $\theta = 0$ (oriented horizontally) and left to right $\kappa = 10^{-1}$, 10^{1} and 10^{3}. *Middle*: Principal orientation field, θ_p, as measured by the image analysis method of a single patch. *Bottom*: Alignment magnitude field, $\|\boldsymbol{T}\|$, as measured by the image analysis method of a single patch.

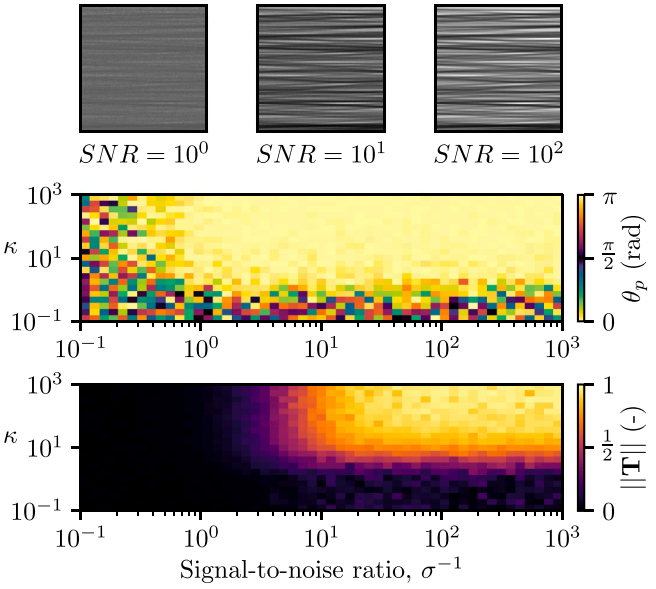

Fig. 4. Effect of speckle on the image analysis technique for idealised fibres. *Top*: Three examples of artificial radiographs of idealised fibre orientation profiles with principal angle of $\theta = 0$, alignment of $\kappa = 10^{3}$ and varying speckle level left to right of $\sigma = 10^{0}$, 10^{-1} and 10^{-2}. *Middle*: Principal orientation field, θ_p, as measured by the image analysis method of a single patch. *Bottom*: Alignment magnitude field, $\|\boldsymbol{T}\|$, as measured by the image analysis method of a single patch.

$$\boldsymbol{T} = \sqrt{2}\left(\frac{\sum_{\boldsymbol{k}} S(\boldsymbol{k})\boldsymbol{Q}(\boldsymbol{k})}{\sum_{\boldsymbol{k}} S(\boldsymbol{k})} - \frac{\boldsymbol{I}}{2}\right), \tag{4}$$

where $\boldsymbol{I}$ is the identity matrix. This nematic order tensor $\boldsymbol{T}$ has the property that its magnitude $\|\boldsymbol{T}\|$ is zero when the power spectrum is isotropic (e.g. when fibres are distributed isotropically) and is one when all of the energy in the power spectrum is aligned in one direction (e.g. for an image that contains only fibres which are perfectly aligned). This magnitude $\|\boldsymbol{T}\|$ is referred to as the *alignment magnitude*. Additionally, by calculating the eigenvectors of this tensor, the *principal orientation*, θ_p, of the power spectrum is recovered in the given patch, which is taken to be the direction of the principal alignment of the fibres. A graphical summary and further explanation of this method is shown in Fig. 2 of Guillard et al. [54].

Three simple examples are represented in Fig. 2 to illustrate the performance of the image analysis technique. In the first example, a black and white image with a spiral was processed for various patch widths w. The principal orientation θ_p and alignment magnitude $\|\boldsymbol{T}\|$ fields are shown for each of these patch widths. Robust and stable measurements of the orientation of the spiral are recovered when the patch size is large enough to cover more than one arm of the spiral. When the patches are smaller than this limit, the measured orientation field either measures the orientation of the only spiral part in the image or nothing, depending on the content of the patch. In this instance, a spatial map of the presence of the spiral and its orientation is recovered. Note that the size of the patches has a significant effect on the measured result. Larger patches produce smoother, more continuous fields. As is common with all up-scaling methods (i.e. making continuum measurements from micro-scale data), a length scale must be chosen over which to make this continuum assumption. In this case, that length scale is related to the size of the patch.

The second and third simple examples show the performance with idealised images of radiographs of fibres. These images were produced by randomly positioning line elements that are semi-transparent. The technique is able to recover both the principal orientation and alignment magnitude of the images for a wide range of patch sizes. It should be noted that at the edges of these images when the patches protrude beyond the image boundaries, the patches are filled with a value of 0, and the results become less valid. This becomes more visible with the larger patch widths. For all experimental data reported in Section 4 the analysed patches are fully within the observed experimental domain.

2.2. Validation of measured fibre orientation

To assess the performance of the imaging processing technique quantitatively, idealised fibre radiographs were produced with known fibre orientations based on the circular von Mises probability density function:

$$P(\theta, \kappa) = \frac{e^{\kappa cos\theta}}{2\pi I_0(\kappa)}, \tag{5}$$

where θ is the orientation of the fibres, κ is a parameter representing the alignment, and I_0 is the modified Bessel function of order zero. This probability density function has the advantage that at $\kappa = 0$, the fibres have an isotropic distribution, and at $\kappa = \infty$, the fibres are perfectly aligned in the direction θ. In Fig. 3, the performance of the image analysis algorithm is shown for a wide range of κ for a single patch. Examples of those patches are given at the top of the Figure. It should be noted that the performance would only increase after averaging over many patches.

Additionally, an investigation of the level of noise in the image (speckle) is presented in Fig. 4. Noise is present in all images, and can come from a variety of sources, including fluctuations in X-ray intensity, scattering of X-rays, and noise in the detector panel. Normally distributed noise was added to each pixel of the generated images of artificial radiographs as:

$$F^{\text{speckled}} = \frac{F}{\overline{F}} + \frac{e^{-\frac{1}{2}\left(\frac{X}{\sigma}\right)^2}}{\sigma\sqrt{2\pi}}, \tag{6}$$

where σ is the width of the normal distribution, X is a random variable

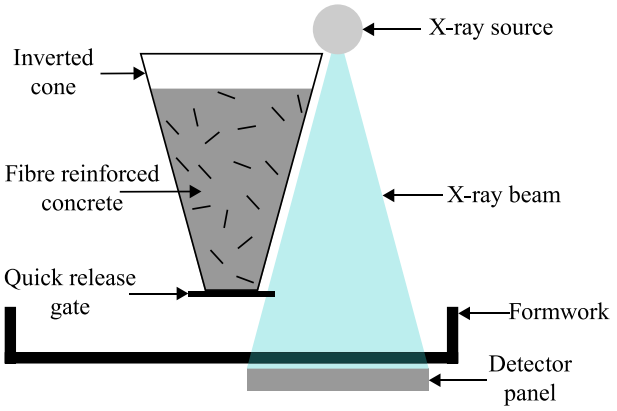

Fig. 5. Schematic representation of the pouring and monitoring scheme. The X-ray source is mounted vertically above the formwork and detector panel.

and $\overline{F}$ is the mean of the artificial radiograph F. The signal-to-noise ratio (SNR) is defined for this case as SNR $= \frac{1}{\sigma}$. The measurement of the principal fibre orientation and alignment magnitude are shown in Fig. 4 to be insensitive to the noise level as long as SNR $\gtrapprox$ 1 and 10, respectively. This means that even when fibres are visually very hard to identify, e.g. for SNR $\approx$ 1, the algorithm still provides adequate results.

3. Experimental programme

The flowability of cementitious composite is one important factor affecting fibre orientation [29]. During pouring, fibres are often assumed to be distributed isotropically within cementitious composite [27]. However, elongated particles, in general, are known to reorient due to several factors such as wall effects [57], and alignment induced by a flow field [58]. Several authors have observed that when the flow is radial, fibres orient perpendicular to the direction of radial flow [28–30]. Alternatively, when concrete flows parallel to the edges of the formwork, fibres reorient in the direction of the flow [11,30,59].

The reorientation of fibres is more pronounced in flows with higher velocity and is therefore related to the casting rate and potential energy [12]. Although the time taken for fibres to reorient has been reported to be considered instantaneous on a larger scale [6], this follows an inverse relation relative to the shear rate of cementitious composite flow [11]. It was found through simulated models that fibre reorientation increased with flow duration [28]. However, no experimental studies detailing the continuous change in fibre orientation are available without resorting to the substitution of cementitious composite with a material model [30]. Therefore, the experimental programme developed in this section was designed to monitor the fibre orientation in concrete slabs while pouring. Both velocity measurements and the algorithm proposed in Section 2 are used in conjunction to analyse the fibre behaviour. In the following, a description of the image acquisition, specimen dimensions, nomenclature, and materials used is presented.

3.1. Image acquisition

The experiments were conducted in the DynamiX laboratory at The University of Sydney, Australia. During pouring, cementitious composite specimens were exposed to an X-ray flux from a Spellman XRV Generator at 180 keV and a current of 2 mA. The source was positioned vertically above the specimens, such that X-rays would pass downwards through the sample. The X-ray intensity was recorded on a PaxScan 2520DX detector at a spatial resolution of 960 × 768 px and at a temporal resolution of 30 frames per second, positioned as shown in Fig. 5. The radiographs produced by this method were processed using the routines described earlier to recover measurements of particle orientation fields and their evolution over time. Velocity analysis was also performed by examining the bulk behaviour of the medium.

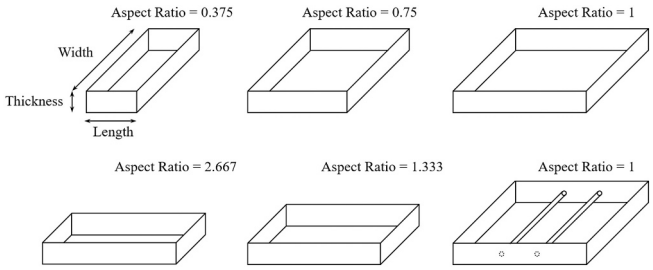

Fig. 6. Specimen geometries investigated in this work.

Table 2
Specimen notation. The thickness of all samples was 50 mm.

Specimen	Length (mm)	Width (mm)	Rebars	Aspect ratio
C0.375	150	400	–	0.375
C0.750	300	400	–	0.750
C1.0	400	400	–	1.000
R1.0	400	400	✓	1.000
S1.333	400	300	–	1.333
S2.667	400	150	–	2.667

3.2. Specimen dimensions and nomenclature

Several factors were considered when setting specimen dimensions for this study, including the specimens investigated by other authors [3,16,18,29,31–34] and the specific constraints of the X-ray laboratory (e.g., size of panels and X-ray penetration). Table 1 summarises some of the studies found in the scope of SCC FRC, including specimen dimensions and fibre properties.

Based on the constraints mentioned above, a maximum dimension of 400 mm was set to assure enough area could be monitored during the tests given that the available panels cover 200 × 300 mm^2. The maximum thickness (or height) of the slab, was also set at 50 mm to allow adequate X-ray penetration and good image quality. The adopted fibres were 35 mm in length providing a slab thickness to fibre length ratio of about 1.5. The fibres selected could constrain the free rotations in the vertical direction. However, this study focused only on 2D flow, in which case the fibre length was deemed acceptable [11]. The adopted fibre length versus thickness of the FRC slab is also representative of several real applications of this composite [60].

A total of six specimens were designed to obtain a wide range of aspect ratios, from compact to slender, i.e. from slab to beam type elements. Three specimens were designed with 400 mm width and 50 mm thickness, and 150, 300 or 400 mm length. The other three specimens had 400 mm length and 50 mm thickness, and 150, 300 or 400 mm width. Two PVC bars of 16 mm diameter were included to recreate the presence of steel rebars in a second specimen with dimensions of 400 × 400 × 50 mm^3. Therefore, a total of five aspect ratios yielded from the specimens selected, as represented in Fig. 6. It is worthwhile denoting that the dimensions selected for the slabs were very similar to the ones reported by Sanal and Zihnioglu [16] (also see Table 1).

The specimens were labelled based on their aspect ratio, in the order of increasing lengths and decreasing widths, as shown in Table 2. Specimens were considered slender (S) for aspect ratios larger than one; and compact (C) for aspect ratios smaller or equal than one. In addition, one specimen contained PVC rebars (R).

3.3. Materials, mix proportions and fibre properties

The self-compacting cementitious composite mix design developed in this study took into account other works, namely

Table 3
Mix design (proportions by weight).

	Water	Cement	Sand	Viscocrete 10	Steel fibres
%	12.5	42.4	41.2	0.63	3.27[a]

[a] Corresponds to volumetric fibre content of 1%.

[3,16,18,29,31–34,61]. In the casting process, CEM I 42.5 R cement from Bastion was used. Furthermore, river sand from Bastion with a density of 1600 kg/m^3 was used as aggregate. Sika Viscocrete 10, a third generation, high range water reducing superplasticiser with a density of 1060 kg/m^3 was added to the cementitious composite mix. Finally, Dramix hooked-end steel fibres with a length of 35 mm, and an aspect ratio of 65 were used. The fibres were manufactured from very high strength steel with a density of 8050 kg/m^3. Table 3 summarises the final cementitious composite mix design.

In the mixing process, all dry components (cement, sand, and fibres) were first mixed together for 1 min for homogeneity. During dry mixing, the superplasticiser was stirred-in with the water for 10 s [16]. The water-superplasticiser mixture was then added to the dry mix in 100 ml intervals. After that, the whole mixture was stirred for an additional 3 min [16,62]. Continuous mixing was maintained, and regular checks were done until reaching the desired consistency.

After mixing, the specimens were cast in lubricated slab moulds represented in Fig. 6 and cylinders. The cylinders were kept in the fog room in adequate curing conditions, after which they were tested for ultimate compressive strength at 28 days of age according to the Model Code 2010 [63]. The average compressive strength of these cylinders was found to be 59.6 MPa. In addition, the fresh mixture was subjected to the 'Slump Flow and T_{500} test' [64]. The slump diameter for all mixtures reached 500 mm for an average 4.4s and a maximum average diameter of 629 mm.

4. Results and discussion

4.1. Concrete flow

The total pouring time lasted, on average, about 23 s and was recorded over approximately 700 frames. For analysis, examples of the radiographs recorded for a single test are shown in Fig. 7.

Flow streamlines were obtained using a particle image velocimetry technique [65] (alternatively referred to as digital image correlation). This technique is commonly used in fluid, soil and structural mechanics to characterise the deformation of materials orthogonal to an optical imaging plane. The same technique can be applied to radiographs to recover the velocity field in the imaging plane, but in this instance the measured velocity is the median velocity of the material in the X-ray beam direction [54,66,67]. In this work, the radiographs were split into

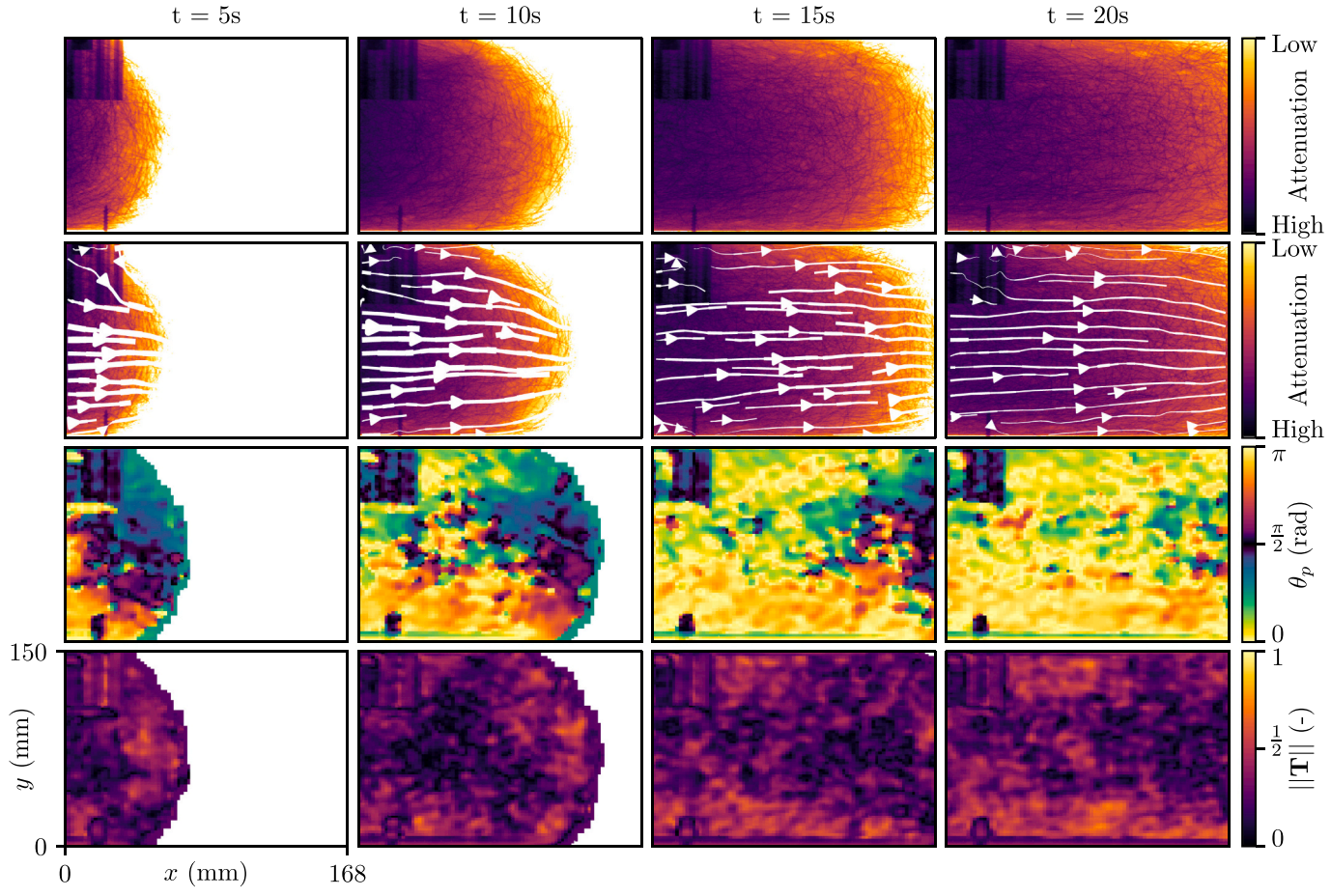

Fig. 7. Processed experimental data for S2.667 at four times. Flow is in the positive x direction. (left to right) with formwork at $y = 0$ and 150 mm. *Left to right*: Time from first material being observed in viewing window is $t = 5$, 10, 15 and 20 s. *Top row*: Attenuation field of X-ray radiographs showing the movement of the FRC from left to right. Fibres are the darker lines spread through the cementitious composite mixture. Dark rectangular areas in the bottom left and top left corners of each image are related to the quick release gate mechanism and should be ignored. *Second row*: Velocity field represented as streamlines overlaid over the radiographs. Thickness of the streamline is proportional to the local speed of the flow. *Third row*: Principal orientation of fibres. Colour represents the principal orientation, where an angle of angle of 90° represents fibres aligned vertically (perpendicular to the bulk flow), and 0° and 180° represent fibres aligned horizontally on the printed page (parallel to the bulk flow). *Bottom row*: Alignment magnitude field.

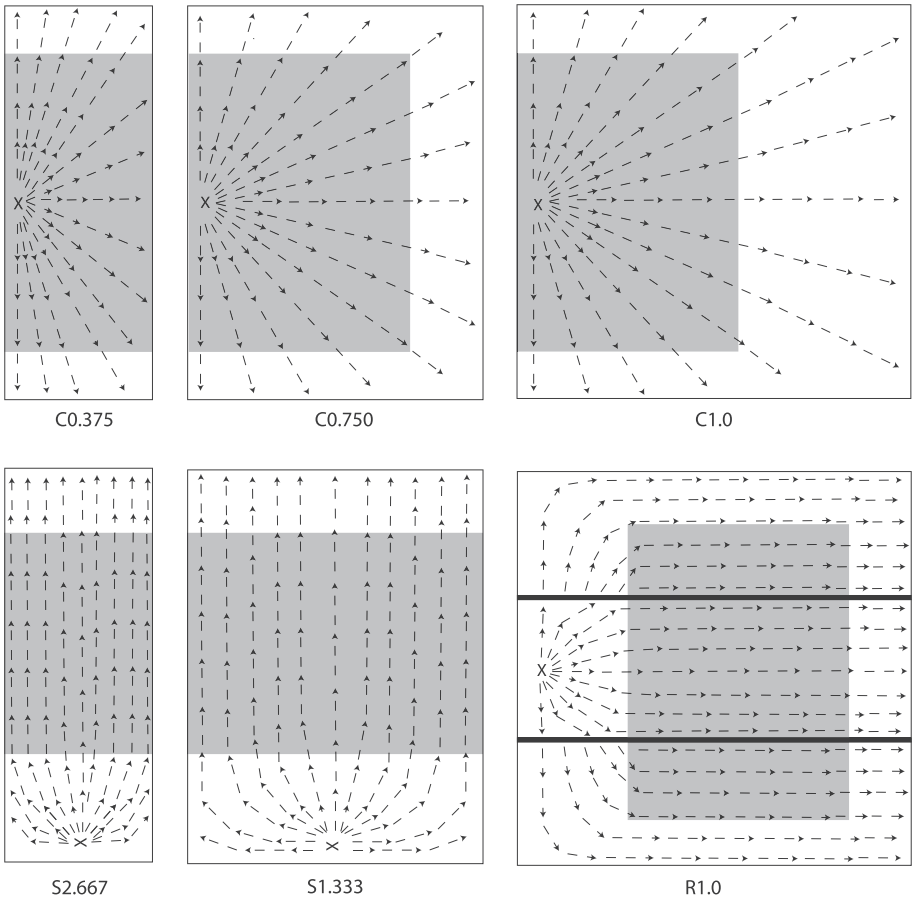

Fig. 8. Schematic representation of the velocity field of the cementitious composite flow. Grey regions mark the location of the detector panel. Data outside of these areas have been inferred. Solid black lines represent reinforcing bars in R1.0.

a number of smaller interrogation patches. Images were pre-processed by digitally removing the formwork from the radiographs and were post-processed to remove statistical outliers in the velocity field. Each pair of images was then compared at times t_0 and $t_0 + \Delta t$ to identify the displacement of the patches travelled during the time interval. The process was repeated for all image pairs and identified patches. The final velocity field in mm/s was computed by using the pixel size and time difference for recorded images. In this study, patches of 32 pixels with an overlap of 50% were analysed with images recorded at 30 frames per second ($\Delta t = \frac{1}{30}$ seconds). As with the fibre orientation measurement, the smoothness of the measured velocity field depends on the patch size.

For ease of understanding, a schematic representation of the streamlines is represented in Fig. 8. Note that in each image, 'X' marks the pouring location, and the streamlines illustrate the progression of the flow from the pouring point. In addition, the grey square denotes the area monitored by the X-ray detector panel. The observed flow was qualitatively consistent with those obtained in Ferrara et al. [3], Sanal and Zihnioglu [16].

As a general observation, radial flow was found at the pouring point for all compact specimens and flow continued radial throughout observed areas if the width was not constrained by formwork edges. As the aspect ratio increased from 0.375 to 1 through increasing specimen length, there was no significant effect on flow. This was observed by Deeb et al. [28] in slump-flow simulations of fibre reinforced cementitious composite, and by Barnett et al. [27] on circular slabs poured from a central point.

A significant effect from the formwork edges on flow was found for aspect ratios greater than 1, similar to Ferrara et al. [3]. Even though the flow could not be observed at the pouring point since it was outside of the X-ray monitored area, the flow in slender specimens was found to be parallel to the specimen length in all cases.

The reinforcement bars had an apparently comparable effect on the cementitious composite flow to constraining the width of the specimen. For example, compare the flow found in R1.0 and C1.0. The addition of the reinforcement caused the cementitious composite flow to become parallel to the bars and formwork instead of flowing radially from the pouring point. In addition, a significantly higher cementitious composite flow velocity is noted in the specimen section within the rebars compared to the section without the rebars. Such results are in agreement with the observations reported by Zirgulis et al. [22]. However, despite the observed flow, as it will be discussed next, the fibre distribution in the central region of this the specimen shows that there was vertical flow of fibres across the rebars, which means that the width of the specimen was not sufficiently constrained by the rebars.

4.2. Ultimate fibre orientation

An example output of the technique described earlier for retrieving fibre orientation is shown in Fig. 7 for S2.667. In this figure, the average orientation of fibres was calculated from 64 × 64 pixel patches of the original images. This patch size was chosen such that sufficient fibres were imaged in each patch to produce relatively smooth results. The choice of this patch size is relatively arbitrary, with a trade-off between spatial resolution and homogeneity. This figure shows the average orientation within each patch, where an angle of 90° represents fibres aligned vertically, and 0° and 180° represent fibres aligned horizontally on the printed page. From analysing such data for all specimens, diagrams were prepared to illustrate the main findings concerning the

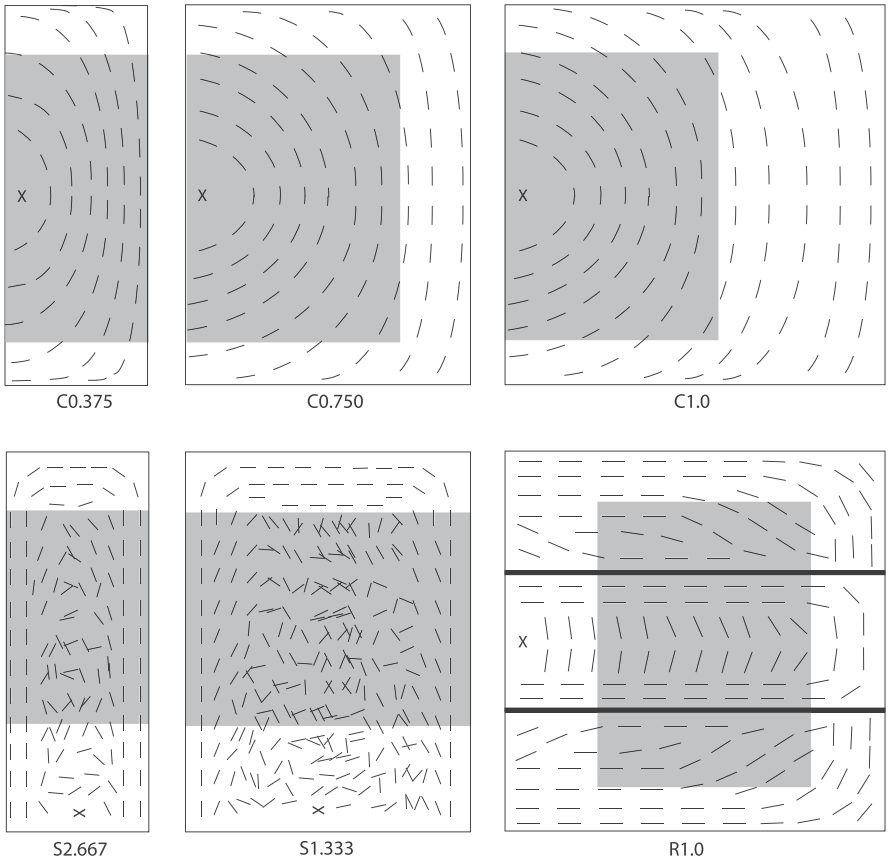

Fig. 9. Schematic representation of the impact of the formwork aspect ratio and position of reinforcing bars on the fibre orientation profile. Grey regions mark the location of the detector panel. Data outside of these areas have been inferred. Solid black lines represent reinforcing bars in R1.0.

ultimate fibre orientation profile — see Fig. 9. Similarities were found in fibre orientation among specimens of the same category, i.e., compact and slender. There were, however, important differences between those as will be discussed ahead.

Fibres were generally oriented radially, perpendicular to the direction of flow in compact specimens, whereas, for slender specimens, two distinct orientations were identified: parallel to flow when close to formwork edges and isotropic when in the central region away from the formwork. When rebars were present, the radial orientation was disrupted, as fibres aligned parallel to the flow in their neighbourhood.

The alignment of fibres perpendicular to the flow was consistent with those registered by Ferrara et al. [3], Barnett et al. [27], Deeb et al. [28], Abrishambaf et al. [29], Boulekbache et al. [30]. The orientation of fibres perpendicular to the flow in compact specimens can be explained by the differences in the velocity field observed in these cases. When the flow is principally radial, the strain rate field is such that the material is being extended in the orthoradial direction. There is a strong effect of this extensional orthoradial flow, which causes fibres to align orthoradially (perpendicular to the radial flow). This effect has been referred to as 'extensional stresses induced orientation' by Svec et al. [68] and modelled for continua of elongated particles in Nadler et al. [58].

The effect of shearing near formwork boundaries was also found to control the ultimate fibre orientation in slender specimens. This flow was dominated by boundary layers, which formed as cementitious composite flowed parallel to the longer formwork edges, as shown in Fig. 9. The properties of this boundary layer are known to depend on the viscosity of cementitious composite [3]. In this case, fibres were observed to align generally subparallel (close to parallel) to the flow.

Near formwork edges, in both slender and compact specimens, the orientation of the fibres was also influenced by the wall effect. This effect is a geometrical constraint forcing fibres to align parallel to the formwork edge if their centroid is at a distance less than half the fibre length [11]. The above shear-induced effects are typically coupled with these wall effects, and in many cases, dominate over wall effects, thus resulting in stronger fibre alignment parallel to formwork edges [11]. A comparison of S2.667 and S1.333 showed that the parallel alignment near the formwork was more noticeable in the first specimen, given that the width was 150 mm compared to 300 mm in the second specimen.

There exists a plug-zone in the central region of slender specimens where the velocity gradient of cementitious composite was low. Within that area, the fibres were dragged without any torque, in which case they remained isotropic [11]. Such an area is quite noticeable in S1.333 and S2.667. For instance, in Fig. 7 for S2.667, the bottom row shows darker colours in the alignment magnitude field associated to the central region of the specimen, which is due to the random distribution of fibres. The size of the plug zone depends on the cementitious composite yield stress. However, this parameter could not be measured for the purpose of this work [69].

Boundary layer flow was also found due to the presence of rebars and caused fibres to orientate parallel to both them and formwork edges. However, given that rebars did not entirely constrain the flow in the vertical plane, cementitious composite could indeed flow above and below them. Therefore, radial flow could possibly develop near the formwork bottom, causing fibres to orientate perpendicular to the flow direction. Hence, neither a circumferential (like in C1.0) nor an almost isotropic (like in the central part of the S2.667) distributions were found.

4.3. *Fibre orientation versus time*

Fibre orientations were not constant during pouring. In fact, fibres were observed to progressively reorient while cementitious composite flowed until their final position. In this section, patches were selected in

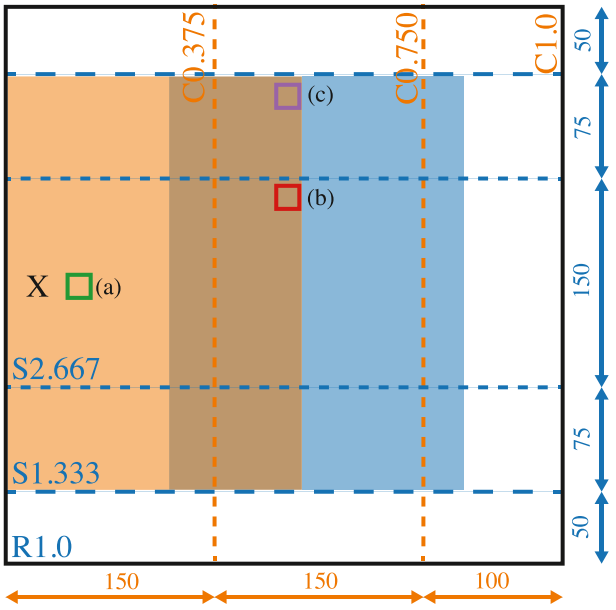

Fig. 10. Location of sampling points for analysis of fibre orientation during pouring. The two detector panel locations are shown in the shaded areas, with correspondingly coloured specimen labels. All dimensions are in mm. The common pouring location is indicated with a X.

commonly imaged areas among the specimens — see Fig. 10: (*i*) green-(a) is horizontally aligned with the pouring point for compact specimens; (*ii*) red-(b) and purple-(c) are located near formwork edges for slender specimens.

The average orientation inside each patch during pouring is represented graphically in Fig. 11. Here we show the magnitude of the difference in angle between the horizontal (as defined in Fig. 9) and the principal orientation. The specimen dimensions compared in each graph are the same, except that, relatively to the pouring, one specimen is compact, and the other is slender or contains rebars.

Fibre orientations inside the patch closest to the pouring point (green-(a)) remained generally above 65° – see Fig. 11(a) and did not change significantly with time. Therefore, the fibres remained approximately perpendicular to the flow during pouring.

The red-(b) curve in Fig. 11(a) represents the patch analysed close to the edge of S2.667. Alternatively, the patch analysed close to the edge for S1.333 and R1 is represented by the purple-(c) curves in Fig. 11(b)–(c). The realignment of fibres with time was most significant at slab edges, where a drop in the average orientation values was seen. Both specimens S2.667 and S1.333 start with an orientation above 60°, which then progressively reduces to an orientation close to 10 to 15°. This takes about 13 s to occur, which is about half of the duration of pouring. Please note that in related works, an angle of 30° is often considered to be parallel [11].

5. Conclusions

This paper presented an imaging technique that enabled the ability to monitor, in real-time, the changes in fibre orientation while pouring. The technique is robust and insensitive to the agglomeration and interactions of fibres that occur naturally while monitoring. As result, maps of the principal fibre orientation and alignment magnitude for individual images of fibres are produced. A sensitivity analysis of this technique was performed, and it was shown that reliable measurements of the principal fibre orientation were produced for signal-to-noise ratios $\gtrsim 1$.

The new technique investigated the impact of specimen aspect ratios and time/duration of pouring on the average orientation of fibres within steel fibre reinforced self-consolidated cementitious composite. The effect of including a reinforcement bar in the specimen on fibre orientations was also explored. As expected, the flow of cementitious composite has a strong effect in inducing preferential fibre alignment within the cementitious composite slabs. It was found that fibres may change orientation progressively over time. Fibres near slab edges can take some time to align parallel to the flow, with the orientation changing progressively from perpendicular to the flow. In the observed slender samples, this could take about half of the total duration of pouring. Such a finding could not be obtained with any other monitoring techniques currently available. This anticipates the possibility of developing strategies to control fibre orientation based on the location of pouring point and duration of pouring.

CRediT authorship contribution statement

Benjy Marks: Conceptualisation, Investigation, Software, Visualization, Validation, Methodology, Writing – Review & Editing.

Marta Miletic: Conceptualisation, Investigation, Methodology, Writing – Review & Editing.

Bernard Lee: Formal analysis, Investigation, Writing – Original Draft.

Hazim Zia: Formal analysis, Investigation, Writing – Original Draft.

Joaquim Barros: Conceptualisation, Methodology, Writing – Review & Editing.

Daniel Dias-da-Costa: Conceptualisation, Investigation, Supervision, Methodology, Writing – Review & Editing.

Declaration of competing interest

The authors declare that they have no known competing financial interests or personal relationships that could have appeared to influence the work reported in this paper.

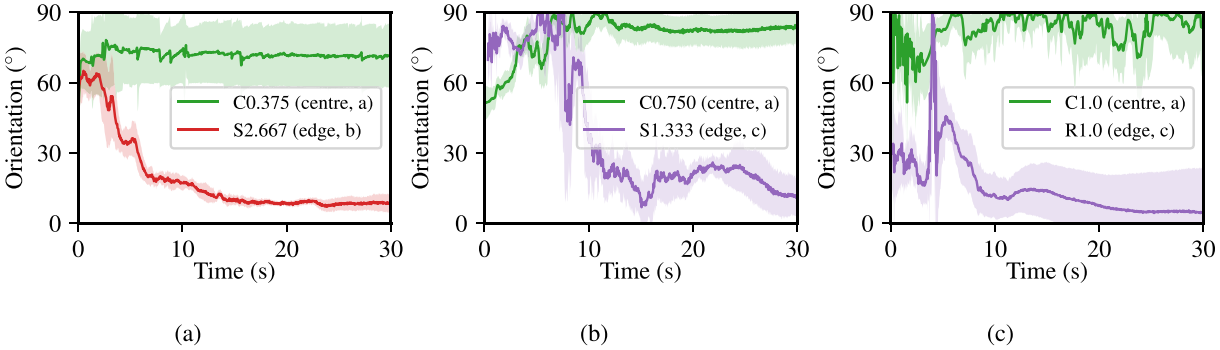

Fig. 11. Fibre orientation versus time for different aspect ratios: (a) 0.357 and 2.667; (b) 0.750 and 1.333; and (c) 1.0. In this case only, fibre orientation is defined to be at 0° when fibres are parallel to the flow direction, and 90° when fibres are perpendicular to the flow direction.

Acknowledgements

B. Marks would like to thank F. Guillard and B. Nadler for thought provoking discussions. The authors would like to acknowledge the University of Sydney for supporting the undergraduate project, as well as the structural laboratory staff. D. Dias-da-Costa would like to acknowledge the support from the University of Sydney through the Sydney Research Accelerator (SOAR) programme.

References

[1] R. Deeb, A. Ghanbari, B. Karihaloo, Development of self-compacting high and ultra high performance concretes with and without steel fibres, Cement & Concrete Composites 34 (2012) 185–190.
[2] P. Mangat, Tensile strength of steel fiber reinforced concrete, Cem. Concr. Res. 6 (1976) 245–252.
[3] L. Ferrara, N. Ozyurt, M. di Prisco, High mechanical performance of fibre reinforced cementitious composites: the role of “casting-flow induced” fibre orientation, Mater. Struct. 44 (2011) 109–128.
[4] T. Simões, C. Octávio, J. Valença, H. Costa, D. Dias-da-Costa, E. Júlio, Influence of concrete strength and steel fibre geometry on the fibre/matrix interface, Composites Part B 122 (2017) 156–164.
[5] T. Simões, H. Costa, D. Dias-da-Costa, E. Júlio, Influence of type and dosage of micro-fibres on the physical properties of fibre reinforced mortar matrixes, Constr. Build. Mater. 187 (2018) 1277–1285.
[6] M.G. Alberti, A. Enfedaque, J.C. Gálvez, A review on the assessment and prediction of the orientation and distribution of fibres for concrete, Compos. Part B 151 (2018) 274–290.
[7] R. Zerbino, J. Tobes, M. Bossio, G. Giaccio, On the orientation of fibres in structural members fabricated with self-compacting fibre reinforced concrete, Cement & Concrete Composites 34 (2012) 191–200.
[8] H. Toutanji, Z. Bayasi, Effects of manufacturing techniques on the flexural behaviour of steel fiber-reinforced concrete, Cem. Concr. Res. 28 (1998) 115–124.
[9] R. Deeb, B.L. Karihaloo, S. Kulasegaram, Reorientation of short steel fibers during the flow of self-compacting concrete mix and determination of the fiber orientation factor, Cem. Concr. Res. 56 (2014) 112–120.
[10] A. Abrishambaf, J.A. Barros, V.M. Cunha, Relation between fibre distribution and post-cracking behaviour in steel fibre reinforced self-compacting concrete panels, Cem. Concr. Res. 51 (2013) 57–66.
[11] L. Martinie, N. Roussel, Simple tools for fiber orientation prediction in industrial practice, Cem. Concr. Res. 41 (2011) 993–1000.
[12] E. Jasiuniene, V. Cicenas, P. Grigaliunas, Z. Rudzionis, A.A. Navickas, Influence of the Rheological Properties on the Steel Fibre Distribution and Orientation in Self-Compacting Concrete, Materials and Structures 51, 2018.
[13] Y. Zhang, D. Dias-da-Costa, Seismic vulnerability of multi-span continuous girder bridges with steel fibre reinforced concrete columns, Eng. Struct. 150 (2017) 451–464.
[14] S.-T. Kang, J.-K. Kim, Numerical simulation of the variation of fiber orientation distribution during flow molding of ultra high performance cementitious composites (UHPCC), Cement & Concrete Composites 34 (2012) 208–217.
[15] M. Carvalho, J. Barros, Y. Zhang, D. Dias-da-Costa, A computational model for simulation of steel fibre reinforced concrete with explicit fibres and cracks, Comput. Methods Appl. Mech. Eng. 363 (2020) 112879.
[16] I. Sanal, N.Ö. Zihnioglu, To what extent does the fiber orientation affect mechanical performance? Constr. Build. Mater. 44 (2013) 671–681.
[17] R.S. Olivito, F.A. Zuccarello, An experimental study on the tensile strength of steel fiber reinforced concrete, Compos. Part B 41 (2010) 246–255.
[18] J. Andries, P. Van Itterbeeck, L. Vandewalle, A. Van Geysel, Influence of Concrete Flow on Spatial Distribution and Orientation of Fibres in Steel Fibre Reinforced Self-compacting Concrete, in: Fib Symposium, Copenhagen, Denmark, 2015, pp. 1–10.
[19] V. Corinaldesi, G. Moriconi, Characterization of self-compacting concretes prepared with different fibers and mineral additions, Cement & Concrete Composites 33 (2011) 596–601.
[20] D.-Y. Yoo, Y.-S. Yoon, N. Banthia, Flexural response of steel-fiber-reinforced concrete beams: effects of strength, fiber content, and strain-rate, Cem. Concr. Compos. 64 (2015) 84–92.
[21] M. Miletić, D. Perić, Effect of fibers on the onset of strain localization in HPFRCC subjected to plane stress loading, J. Eng. Mech. 144 (2018), 04018074.
[22] G. Zirgulis, O. Svec, M.R. Geiker, A. Cwirzen, T. Kanstad, Influence of reinforcing bar layout on fibre orientation and distribution in slabs cast from fibre-reinforced self-compacting concrete (FRSCC), Structural Concrete 17 (2016) 245–256.
[23] D.Y. Yoo, G. Zi, S.T. Kang, Y.S. Yoon, Biaxial flexural behavior of ultra high performance fiber reinforced concrete with different fiber lengths and placement methods, Cement & Concrete Composites 63 (2015) 51–66.
[24] P. Richard, M. Cheyrezy, Composition of reactive powder concretes, Cem. Concr. Res. 25 (1995) 1501–1511.
[25] R. Gettu, D.R. Gardner, H. Saldívar, B.E. Barragán, Study of the distribution and orientation of fibers in SFRC specimens, Mater. Struct. 38 (2005) 31–37.
[26] J. Spangenberg, N. Roussel, J. Hattel, E. Sarmiento, M. Geiker, Patterns of gravity induced aggregate migration during casting of fluid concretes, Cem. Concr. Res. 42 (2012) 1571–1578.
[27] S.J. Barnett, J.-F. Lataste, T. Parry, S.G. Millard, M.N. Soutsos, Assessment of fibre orientation in ultra high performance fibre reinforced concrete and its effect on flexural strength, Mater. Struct. 43 (2010) 1009–1023.
[28] R. Deeb, B. Karihaloo, S. Kulasegaram, Reorientation of short steel fibres during the flow of self-compacting concrete mix and determination of the fibre orientation factor, Cem. Concr. Res. 56 (2014) 112–120.
[29] A. Abrishambaf, V. Cunha, J. Barros, The Influence of Fibre Orientation on the Post-cracking Tensile Behaviour of Steel Fibre Reinforced Self-compacting Concrete, Volume 31, 2015.
[30] B. Boulekbache, M. Hamrat, M. Chemrouk, S. Amziane, Flowability of fibre-reinforced concrete and its effect on the mechanical properties of the material, Constr. Build. Mater. 24 (2010) 1664–1671.
[31] R. Lameiras, J.A.O. Barros, M. Azenha, Influence of casting condition on the anisotropy of the fracture properties of steel fibre reinforced self-compacting concrete (SFRSCC), Cement and Concrete Composites 59 (2015) 60–76.
[32] P. Stähli, R. Custer, J.G.M. van Mier, On flow properties, fibre distribution, fibre orientation and flexural behaviour of FRC, Mater. Struct. 41 (2008) 189–196.
[33] J.P. Suuronen, A. Kallonen, M. Eik, J. Puttonen, R. Serimaa, H. Herrmann, Analysis of short fibres orientation in steel fibre-reinforced concrete (SFRC) by X-ray tomography, J. Mater. Sci. 48 (2013) 1358–1367.
[34] R. Zerbino, J.M. Tobes, M.E. Bossio, G. Giaccio, On the orientation of fibres in structural members fabricated with self compacting fibre reinforced concrete, Cem. Concr. Compos. 34 (2012) 191–200.
[35] Y. Akkaya, J. Picka, S.P. Shah, Spatial distribution of aligned short fibers in cement composites, J. Mater. Civ. Eng. 12 (2000) 272–279.
[36] J.-L. Chermant, L. Chermant, M. Coster, A.-S. Dequiedt, C. Redon, Some fields of applications of automatic image analysis in civil engineering, Cem. Concr. Compos. 23 (2001) 157–169.
[37] L. Ferrara, A. Meda, Relationships between fibre distribution, workability and the mechanical properties of SFRC applied to precast roof elements, Mater. Struct. 39 (2006) 411–420.
[38] R. Wang, X. Gao, J. Zhang, G. Han, Spatial distribution of steel fibers and air bubbles in UHPC cylinder determined by X-ray CT method, Constr. Build. Mater. 160 (2018) 39–47.
[39] Ł. Skarżyński, J. Suchorzewski, Mechanical and fracture properties of concrete reinforced with recycled and industrial steel fibers using digital image correlation technique and X-ray micro computed tomography, Constr. Build. Mater. 183 (2018) 283–299.
[40] E.E. Underwood, Quantitative stereology, MA, Reading, 1970, p. 5.
[41] J. Lataste, M. Behloul, D. Breysse, Characterisation of fibres distribution in a steel fibre reinforced concrete with electrical resistivity measurements, NDT & E International 41 (2008) 638–647.
[42] N. Ozyurt, L.Y. Woo, T.O. Mason, S.P. Shah, Monitoring fiber dispersion in fiber-reinforced cementitious materials: comparison of ac-impedance spectroscopy and image analysis, ACI Mater. J. 103 (2006) 340.
[43] P. Stroeven, The analysis of fibre distributions in fibre reinforced materials, J. Microsc. 111 (1977) 283–295.
[44] R.S. Bay, C.L. Tucker III, Stereological measurement and error estimates for three-dimensional fiber orientation, Polym. Eng. Sci. 32 (1992) 240–253.
[45] J. Schnell, F. Ackermann, R. Rösch, T. Sych, Statistical Analysis of the Fibre Distribution in Ultra High Performance Concrete Using Computer Tomography, in: Proceedings of the Second International Symposium on UHPC, Kassel, Germany, 2008, pp. 145–152.
[46] M.A. Vicente, D.C. González, J. Mínguez, Determination of dominant fibre orientations in fibre-reinforced high-strength concrete elements based on computed tomography scans, Nondestructive Testing and Evaluation 29 (2014) 164–182.
[47] T. Ponikiewski, J. Katzer, M. Bugdol, M. Rudzki, X-ray computed tomography harnessed to determine 3d spacing of steel fibres in self compacting concrete (scc) slabs, Construction and Building Materials 74 (2015) 102–108.
[48] T. Ponikiewski, J. Gołaszewski, M. Rudzki, M. Bugdol, Determination of steel fibres distribution in self-compacting concrete beams using X-ray computed tomography, Archives of Civil and Mechanical Engineering 15 (2015) 558–568.
[49] T. Ponikiewski, J. Katzer, M. Bugdol, M. Rudzki, Steel fibre spacing in self-compacting concrete precast walls by X-ray computed tomography, Mater. Struct. 48 (2015) 3863–3874.
[50] H. Herrmann, E. Pastorelli, A. Kallonen, J.-P. Suuronen, Methods for fibre orientation analysis of X-ray tomography images of steel fibre reinforced concrete (SFRC), Journal of materials science 51 (2016) 3772–3783.
[51] T. Oesch, E. Landis, D. Kuchma, A methodology for quantifying the impact of casting procedure on anisotropy in fiber-reinforced concrete using X-ray CT, Mater. Struct. 51 (2018) 73.
[52] J.D. Ríos, C. Leiva, M. Ariza, S. Seitl, H. Cifuentes, Analysis of the tensile fracture properties of ultra-high-strength fiber-reinforced concrete with different types of steel fibers by X-ray tomography, Mater. Des. 165 (2019) 107582.
[53] M. Miletić, L.M. Kumar, J.-Y. Arns, A. Agarwal, S.J. Foster, C. Arns, D. Perić, Gradient-based fibre detection method on 3d micro-CT tomographic image for defining fibre orientation bias in ultra-high-performance concrete, Cem. Concr. Res. 129 (2020) 105962.
[54] F. Guillard, B. Marks, I. Einav, Dynamic X-ray radiography reveals particle size and shape orientation fields during granular flow, Sci. Rep. 7 (2017) 8155.
[55] S. Jiang, L. Shen, F. Guillard, I. Einav, Fracture and fragmentation patterns within a single cemented glass bead under impact, International Journal of Impact Engineering 131 (2019) 152–161.
[56] N. J. Mottram, C. J. Newton, Introduction to q-tensor Theory, arXiv Preprint arXiv: 1409.3542 (2014).

[57] D. Dupont, L. Vandewalle, Distribution of Steel Fibres in Rectangular Sections, Volume 27, 2005.
[58] B. Nadler, F. Guillard, I. Einav, Kinematic model of transient shape-induced anisotropy in dense granular flow, Phys. Rev. Lett. 120 (2018) 198003.
[59] F. Laranjeira, S. Grünewald, J. Walraven, C. Blom, C. Molins, A. Aguado, Characterization of the orientation profile of steel fiber reinforced concrete, Mater. Struct. 44 (2011) 1093–1111.
[60] J. Barros, Fiber Reinforced Concrete and Glass Fibre Reinforced Polymer Systems for the Development of More Sustainable Construction Systems, BEFIB 2016, 9th Rilem International Symposium on Fiber Reinforced Concrete, Vancouver, Canada (19–21), September 2016.
[61] J. Michels, D. Waldmann, S. Maas, A. Zürbes, Steel fibers as only reinforcement for flat slab construction - experimental investigation and design, Constr. Build. Mater. 26 (2012) 145–155.
[62] N. Ozyurt, T.O. Mason, S.P. Shah, Non-destructive monitoring of fiber orientation using ac-is: an industrial-scale application, Cem. Concr. Res. 36 (2006) 1653–1660.
[63] fib, Model Code for Concrete Structures 2010, Berlin: Wiley-VCH (2013).
[64] WSDOT, C1611/C1611M-18 Standard Test Method for Slump Flow of Self-Consolidating Concrete, Technical Report, ASTM International, 2018.
[65] W. Thielicke, E, Stamhuis, Pivlab, Towards user-friendly, affordable and accurate digital particle image velocimetry in matlab, 2014.
[66] A. Fouras, J. Dusting, R. Lewis, K. Hourigan, Three-dimensional synchrotron x-ray particle image velocimetry, J. Appl. Phys. 102 (2007), 064916.
[67] J. Baker, F. Guillard, B. Marks, I. Einav, X-ray rheography uncovers planar granular flows despite non-planar walls, Nat. Commun. 9 (2018) 1–9.
[68] O. Svec, G. Zirgulis, J.E. Bolander, H. Stang, Influence of formwork surface on the orientation of steel fibres within self-compacting concrete and on the mechanical properties of cast structural elements, Cem. Concr. Compos. 50 (2014) 60–72.
[69] K.H. Khayat, G. De Schutter (Eds.), Mechanical Properties of Self-compacting Concrete, Volume 14 of RILEM State-of-the-Art Reports, Springer, 2014, https://doi.org/10.1007/978-3-319-03245-0. URL.